How to cite: *Angew. Chem. Int. Ed.* **2021**, *60*, 10155–10163
International Edition: doi.org/10.1002/anie.202016653
German Edition: doi.org/10.1002/ange.202016653

Lewis Acids | Hot Paper

Activation of 2-Cyclohexenone by BF_3 Coordination: Mechanistic Insights from Theory and Experiment

Martin T. Peschel[+], Piotr Kabaciński[+], Daniel P. Schwinger, Erling Thyrhaug, Giulio Cerullo, Thorsten Bach, Jürgen Hauer, and Regina de Vivie-Riedle**

Abstract: *Lewis acids have recently been recognized as catalysts enabling enantioselective photochemical transformations. Mechanistic studies on these systems are however rare, either due to their absorption at wavelengths shorter than 260 nm, or due to the limitations of theoretical dynamic studies for larger complexes. In this work, we overcome these challenges and employ sub-30-fs transient absorption in the UV, in combination with a highly accurate theoretical treatment on the XMS-CASPT2 level. We investigate 2-cyclohexenone and its complex to boron trifluoride and analyze the observed dynamics based on trajectory calculations including non-adiabatic coupling and intersystem crossing. This approach explains all ultrafast decay pathways observed in the complex. We show that the Lewis acid remains attached to the substrate in the triplet state, which in turn explains why chiral boron-based Lewis acids induce a high enantioselectivity in photocycloaddition reactions.*

Introduction

Lewis acids modulate the photochemical behavior of carbonyl compounds by coordination to the Lewis-basic oxygen atom. Although the fact that Lewis acids can have a beneficial impact on the course of photochemical reactions has been known for more than a century,[1] systematic studies of the interaction between a Lewis acid and a carbonyl chromophore were first undertaken in the 1980s and 1990s. Among several notable contributions,[2] the topic was most comprehensively investigated by the groups of Lewis and Fukuzumi. Lewis and co-workers explored the photochemistry of coumarins, quinolones, cinnamates and related compounds in a series of papers entitled "Lewis Acid Catalysis of Photochemical Reactions".[3] The group of Fukuzumi interrogated the influence of a Lewis acid on the photoredox properties of carbonyl compounds[4] in the context of their general interest in the effect of Lewis acids on photoredox catalysis.[5] In more recent years, the interest in Lewis acids and carbonyl compounds has been largely triggered by the desire to exploit chiral Lewis acids for the enantioselective catalysis of photochemical reactions.[6] The [2+2] photocycloaddition attracted the most attention and several modes of action were shown to be operative, including (a) a stabilization of the excited state,[7] (b) a more facile photoredox event,[8] (c) a bathochromic absorption shift,[9] (d) a lowering of the energy of the triplet state[10] or combinations thereof.[11] Apart from the enantioselectivity issue, Lewis acids have also been found to be useful to activate aromatic carbonyl compounds towards a reaction at the aromatic or heteroaromatic core.[12] They may also allow for new reaction pathways, such that reactions can take place in a different spin state.[13]

Several experimental studies were accompanied[10,11,12a,13,14] or supported[15] in separate papers by calculations which aided to understand the course of the reaction. However, despite the increasing number of synthetic studies, very little attention has been paid to the immediate influence of the Lewis acid on a carbonyl chromophore upon excitation. Despite early laser flash photolysis studies on relevant carbonyl compounds, e.g. cyclic α,β-unsaturated ketones (enones),[16] an elemental picture of the fate of a typical photochemical substrate in the presence of a Lewis acid does not exist. Previous theoretical studies already addressed the nature of the excited states and reaction paths of simple enones[17–19] and semiclassical dynamics gave insight into the singlet-triplet crossing mechanisms.[20] The reaction paths in Lewis acid complexes have also been investigated computationally, but these studies were focused on different classes of enones (coumarines and 5,6-dihydro-4-pyridones), for which the order of the excited states is different.[15]

Here we present a detailed mechanistic study on the effects of the addition of the Lewis acid BF_3 to the paradigmatic 2-cyclohexenone (**1**), to form the photocatalytic complex (**2**), (Scheme 1). The combination of state-of-the-art femtosecond transient absorption (TA) in the UV and high-

[*] M. T. Peschel,[+] R. de Vivie-Riedle
Department Chemie, Ludwig-Maximilians-Universität München
81377 München (Germany)
E-mail: regina.de_vivie@cup.uni-muenchen.de
P. Kabaciński,[+] G. Cerullo
IFN-CNR and Dipartimento di Fisica, Politecnico di Milano
20133 Milano (Italy)
D. P. Schwinger, E. Thyrhaug, T. Bach, J. Hauer
Department of Chemistry and Catalysis Research Center (CRC),
Technische Universität München
85747 Garching (Germany)
E-mail: juergen.hauer@tum.de
[+] These authors contributed equally to this work.
Supporting information and the ORCID identification number(s) for the author(s) of this article can be found under: https://doi.org/10.1002/anie.202016653.

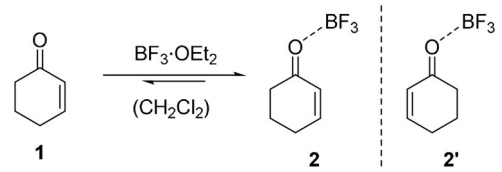

Scheme 1. 2-Cyclohexenone (**1**) as a model substrate to explore the photophysical properties of its Lewis acid complex **2** to boron trifluoride (Isomer **2′** with BF_3 coordinated away from the double bond).

level quantum dynamical and quantum chemical methods on the XMS-CASPT2 level of theory allows us to (a) highlight the effects of Lewis acid addition on both static and dynamic system properties, (b) identify and describe not only the reaction pathway towards the photocatalytically active low-lying triplet state T_1, but also an important loss channel, namely radiationless $S_1 \rightarrow S_0$ internal conversion via a conical intersection.

Results and Discussion

Vertical Excitation Energies and Calculated Absorption Spectra. The 2-cyclohexenone-BF_3 complex (**2**) was generated by treatment of 2-cyclohexenone (**1**) with an excess of $BF_3{\cdot}OEt_2$ in dichloromethane solution. In previous work by Childs et al., complex **2** had been studied by NMR spectroscopy and was identified as a 1:1 complex.[21] Addition of $BF_3{\cdot}OEt_2$ to 2-cyclohexenone led to a bathochromic shift of the strong absorption band at $\lambda = 224$ nm ($\varepsilon = 12.6 \times 10^{-3}$ L mol^{-1} cm^{-1}) to a new signal with a maximum at $\lambda =$ 250 nm. Beyond 5.0 equiv. of $BF_3{\cdot}OEt_2$, the absorbance did not increase further (Figure 1b), indicating complete formation of complex **2** at this concentration. The isosbestic point at $\lambda = 236$ nm revealed that no other species was formed but the 1:1 complex. The weak absorption at $\lambda = 330$ nm observed in **1** ($\varepsilon = 34$ L mol^{-1} cm^{-1}, see Figure 1a) disappeared completely. Instead, a shoulder developed at $\lambda = 266$ nm (Figure 1b).

The large red shift in the absorption spectra of the complex **2** compared to 2-cyclohexenone (**1**) can be explained by inspection of the calculated vertical excitation energies. Starting from the optimized ground state geometry, the excited state energies were calculated on XMS-CASPT2(6,5)/cc-pvtz level of theory for the singlets S_1, S_2 and the triplets T_1 and T_2. In both cases the agreement between theory and experiment is excellent (Table 1).

In the enone **1**, the $S_1(n\pi^*)$ state is almost dark, only the $S_2(\pi\pi^*)$ state exhibits a significant transition dipole moment of 4.53 D (Table 1). Complex **2** exists in two conformers (see Scheme 1 and Figure S7), in which the boron atom resides in the plane of the conjugated π-system and the BF_3 group is oriented either towards or away from the C=C double bond (structure **2**, respectively, **2′** in Scheme 1). Both conformers exhibit very similar energies and nearly identical absorption spectra. All frontier orbitals of **2** involved in the excitation process, π, n, and π*, shown in Figure 2 for one of the conformers, are stabilized with respect to **1**. The n-orbital representing a lone pair orbital of oxygen is most strongly affected as it participates in the σ-bond formation with the Lewis acid BF_3. The partial transfer of electron density from the oxygen to the boron atom lends some oscillator strength to the nπ* transition and causes a strong blue shift of the $S_1(n\pi^*)$ absorption band from 333 nm to 255 nm. The π*-orbital is subject to an intermediate level of stabilization as it is not directly involved in the O–B bond but is localized close to the oxygen atom. The π-orbital is the least stabilized by complex formation, leading to an overall red shift of the $S_2(\pi\pi^*)$ state in the complex.

The absorption spectra are computed as described in the Computational Methods section of the supporting information and are compared to the experimental spectra in Figure 3a for **1** and Figure 3b for **2**. In complex **2**, the S_2 and S_1 bands partly overlap such that the S_1 contribution can be assigned to the shoulder in the experimental spectrum (Figure 3b). Complex formation affects singlet and triplet states in a similar manner. As the two triplet states lie very

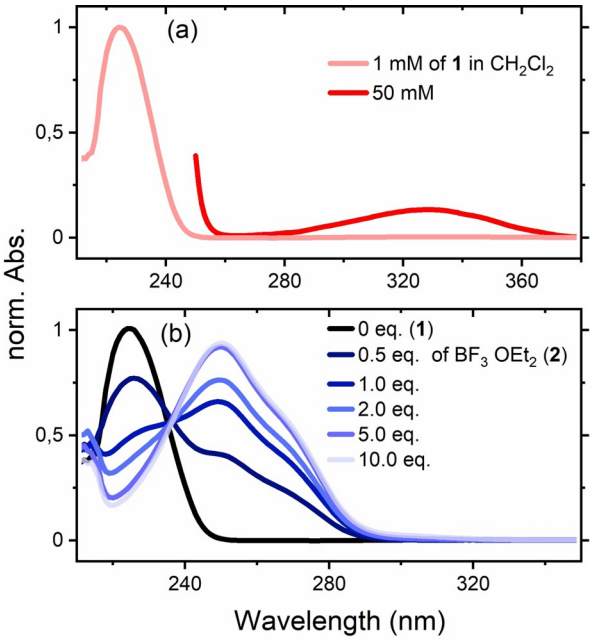

Figure 1. (a) UV/Vis absorption spectrum of 2-cyclohexenone (**1**, CH_2Cl_2, $c = 1.0$ mM, rose; $c = 50$ mM, red) and (b) its variation ($c = 1.0$ mM) upon addition of 0 equiv. (black), 0.5 equiv., 1.0 equiv., 2.0 equiv., 5.0 equiv. and 10.0 equiv. of $BF_3{\cdot}OEt_2$ (formation of **2**, blue).

Table 1: Calculated absorption maxima and transition dipole moments for the lowest two singlet transitions in **1** and **2**. The two values for **2**/ **2′** are for the two different conformers (see Scheme 1 and Figure S7). The absorption maxima of the experimental absorption bands and the shoulder observed in the complex 2 are given in parentheses.

	Excited State	Transition Energy in eV	Transition Wavelength in nm	Transition Dipole in D
1	$S_1(n\pi^*)$	3.73 (3.76)	333 (335)	0.0695
	$S_2(\pi\pi^*)$	5.74 (5.54)	216 (224)	4.53
2/ **2′**	$S_1(n\pi^*)$	4.87/ 4.87 (4.66)	255/ 255 (266)	0.126/ 0.594
	$S_2(\pi\pi^*)$	5.08/ 5.15 (4.96)	244/ 241 (250)	4.93/ 5.06

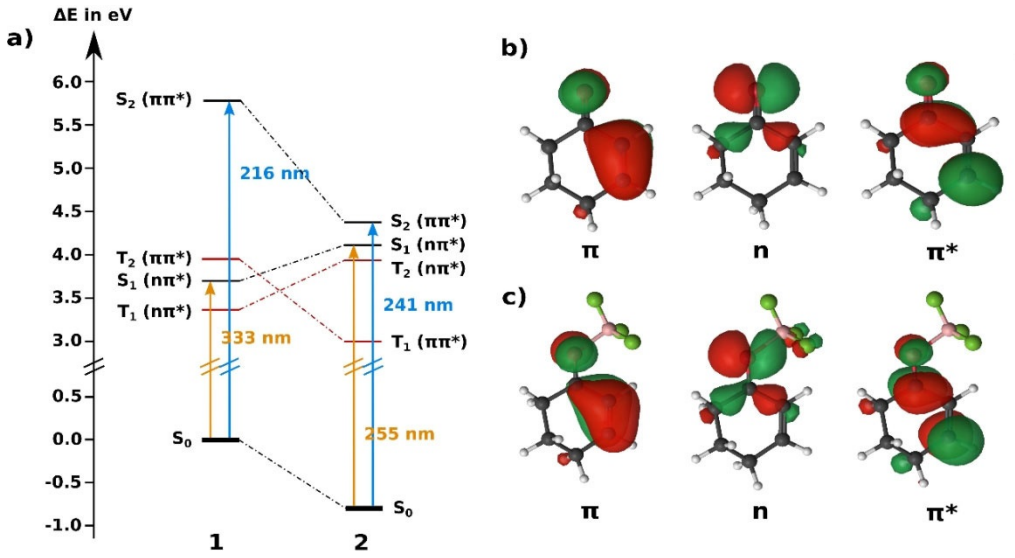

Figure 2. (a) Calculated relative energies of the three lowest singlet and two lowest triplet states at the Franck-Condon point of **1** and **2**. Excitation wavelengths corresponding to the transitions from the ground to the singlet excited states are indicated to allow a direct comparison with the experimental spectra. Orbitals with major contributions to the excitations of **1** and **2** are shown to the right in (b) and (c), respectively.

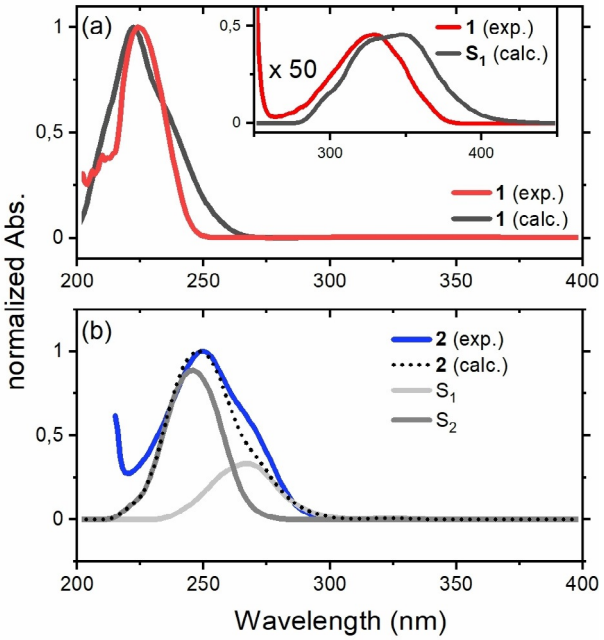

Figure 3. Comparison of the theoretical and experimental UV/Vis spectra. (a) Experimental spectrum of **1** (CH_2Cl_2, $c = 1.0$ mM, $c = 50$ mM in the inset, red), calculated absorption (black) of the $S_1(n\pi^*)$ state (in the inset, multiplied by a factor of 50) and the $S_2(\pi\pi^*)$ state of **1**. (b) Experimental spectrum of **2** (CH_2Cl_2, $c = 1.0$ mM, blue), calculated absorption of the $S_1(n\pi^*)$ state (light grey), the $S_2(\pi\pi^*)$ state (dark grey) and total absorption (black, dotted) of **2**.

close in **1**, complexation leads to a change of character of the T_1 and T_2 states. In both isomers of the complex (**2**/**2′**) T_1 has now $^3(\pi\pi^*)$ character, while T_2 assumes $^3(n\pi^*)$ character. In **1**, the S_1 state is sandwiched between $T_1(n\pi^*)$ and $T_2(\pi\pi^*)$ while in the complex both triplets are located energetically below the S_1 state (see Figure 2a). Significant spin-orbit coupling only occurs between $\pi\pi^*$ and $n\pi^*$ configurations in accordance with El Sayed's rule.[22]

*Reaction Path and Trajectory Calculations for Enone **1**.* Starting from the Franck-Condon (FC) geometry, the $^1(n\pi^*)$ electronic configuration is preserved along the reaction path in the S_1 state. A planar $S_1(n\pi^*)$ minimum could be located as well as two conical intersections (CoIn) with the ground state S_0. At CoIn 1, the ring structure is twisted along the HC=CH dihedral and CoIn 2 is an open ring structure (Figure 4). CoIn 1 lies energetically at the same level as the FC geometry whereas CoIn 2 lies energetically above the FC point (Figure 4, see also Table S5). Hence, no significant transfer through these intersections is expected, instead relaxation might occur via the triplet states. Two minima are found in the adiabatic T_1 potential: the first is planar and of $n\pi^*$ configuration and lies in the FC region, while the second lower one is twisted and of $\pi\pi^*$ configuration (Figure 4). Both minima are connected via a CoIn (T_1T_2 CoIn) and a barrier in its close vicinity. Thus, along the reaction coordinate the $T_2(\pi\pi^*)$ state crosses the $S_1(n\pi^*)$ state. Between these states the spin orbit coupling of 37.96 cm^{-1} is large enough and the energy gap small enough to expect significant intersystem crossing (ISC) from $S_1(n\pi^*)$ to $T_2(\pi\pi^*)$. Thereafter, the $T_2(\pi\pi^*)$ population passes the T_1T_2 CoIn diabatically and becomes $T_1(\pi\pi^*)$, which is long-lived as its spin-orbit coupling to the ground state is small (5.73 cm^{-1}) and the energy gap is large (1.06 eV).

The expectations from the static calculations were verified by trajectory calculations at the XMS-CASPT2(8,7)/cc-pvdz level of theory including non-adiabatic and also spin-orbit coupling. For the dynamics, a smaller double-zeta basis set was employed, which leaves the energetic order of the involved states unaffected at critical points of the potential energy surface (see Tables S6 and S9).

13 Trajectories were started from the S_1 state, ten of which reached the final simulation time of 2 ps. For details see section 6.4 of the supporting information. This small sample

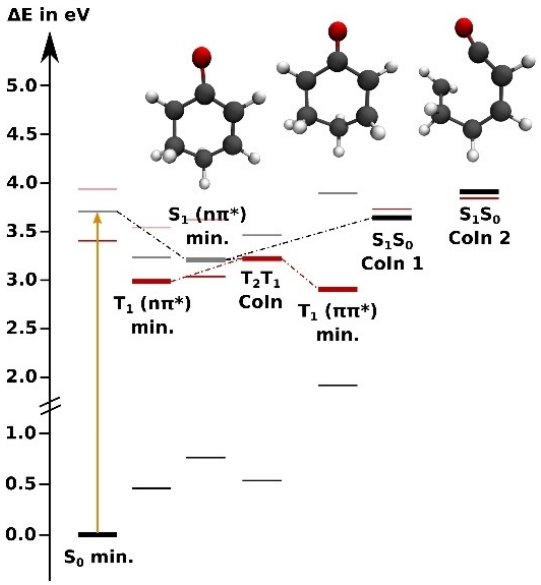

Figure 4. Energy levels of the adiabatic states of **1** at critical points relevant to the relaxation process evaluated on XMS-CASPT2(8,7)/cc-pvdz level of theory. S_0 is shown in black, S_1 in grey; T_1 is shown in red and T_2 in faint red. The thick horizontal lines indicate the energies of the optimized states, while the thin lines indicate the energies of all other states at the optimized geometries (see Tables S5–S10). The dotted lines suggest possible relaxation pathways. The molecular structures are the planar $S_1(n\pi^*)$ minimum (left, slightly elongated C–O bond), the twisted $T_1(\pi\pi^*)$ minimum (middle, torsion around the C–C double bond) and the ring-opening CoIn between S_1 and S_0 (right).

size at a high level of electronic structure theory should give a good picture of the major reaction pathways as all the surviving trajectories show a similar behavior. Only reaction channels of minor importance might be missed. No repopulation of the ground state via either S_1S_0 CoIn 1 or S_1S_0 CoIn 2 was observed, instead, the S_1 state decayed completely to the triplet states with a time constant of approximately 750 fs (Figure 5).

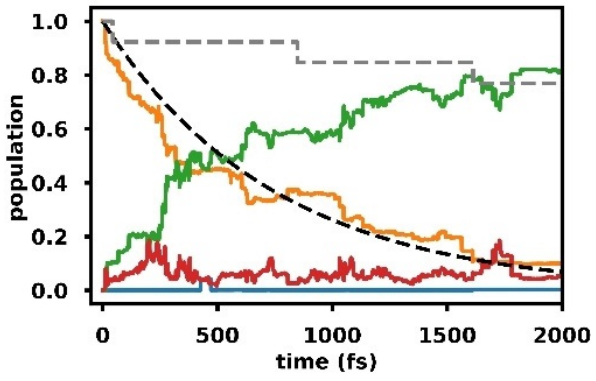

Figure 5. Adiabatic state populations based on quantum amplitudes for XMS-CASPT2(8,7)/cc-pvdz surface hopping trajectories started in the S1 state of **1**; S_1 (orange), S_0 (blue), T_1 (green), T_2 (red), exponential fit of the singlet triplet population transfer with a time constant of 746 fs (black, dashed), fraction of active trajectories (grey, dashed).

This is in good agreement with previous experiments in which a triplet quantum yield close to unity was reported after excitation of 2-cyclohexenone (**1**) to the S_1 state.[16] After subtraction of the backwards crossings, there were in total eleven hops from S_1 to T_2 and eleven hops from T_2 to T_1. All transitions between S_1 and T_2 occurred at nearly planar geometries close to the S_1 minimum. These transitions were associated with a change in the character of the electronic wavefunction from $^1(n\pi^*)$ to $^3(\pi\pi^*)$. Since the T_2T_1 CoIn is also close to the planar geometry, the crossings from $S_1(n\pi^*)$ to $T_2(\pi\pi^*)$ were generally followed immediately by a hop from $T_2(\pi\pi^*)$ to $T_1(\pi\pi^*)$. Accordingly, Figure 5 does not show a significant build-up of population in T_2. The T_1 state can subsequently relax to the $T_1(\pi\pi^*)$ minimum via a twist in the HC=CH dihedral angle. All trajectories that reached the final 2 ps showed some amount of twisting. As no cooling mechanisms were included, they can oscillate quite far away from the triplet minimum due to the large amount of kinetic energy gained along the relaxation path from the FC region which leads to occasional crossings back into T_2.

*Reaction Path and Trajectory Calculations for Complex **2**.* The two conformers **2** and **2′** are energetically very similar with equivalent local and global minima on the potential energy surface. In the following, we will limit our discussion to conformer **2**. In **2**, the FC geometry (Figure 6) is close to a CoIn between S_2 and S_1 (S_2S_1 CoIn). Even an excitation to S_2 will relax very fast to S_1 via the S_2S_1 CoIn, which simultaneously acts as a branching point towards two different pathways.

Preserving the $\pi\pi^*$ character the system reaches a CoIn with the ground state (S_1S_0 CoIn 1) at a twisted geometry. Preserving the $n\pi^*$ character, the system can reach the $S_1(n\pi^*)$ minimum. At this geometry the BF_3 group is rotated out of the molecular plane and the oxygen-boron bond is elongated. This path can lead to heterolytic dissociation of the complex in the gas phase. In this direction another CoIn with the ground state (S_1S_0 CoIn 2) was found with an open ring structure. Thus, in contrast to enone **1** there are two energetically accessible CoIns, and internal conversion can act as a competing channel to ISC. During relaxation into the $S_1(n\pi^*)$ minimum the $T_2(\pi\pi^*)$ state crosses the S_1 state allowing for significant ISC with spin-orbit couplings around 25 cm^{-1}. As in **1**, the T_1 state of **2** displays two minima, one local of $n\pi^*$- and one global of $\pi\pi^*$-character, which are connected by the T_1T_2 CoIn. The $T_1(n\pi^*)$ minimum is geometrically close to the S_1 minimum with the BF_3 group rotated out of plane, while the $T_1(\pi\pi^*)$ minimum is geometrically close to the S_1S_0 CoIn 1 with a twist along the C=C double bond. Compared to the enone reaction path we observe two main differences: close lying and optically addressable S_1 and S_2 states and energetically accessible CoIns with the ground state.

To verify whether the proposed relaxation pathways actually take place in the excited complex **2**, we performed surface hopping calculations at the XMS-CASPT2(8,7)/cc-pvdz level of theory. Due to computational costs, triplet states and spin-orbit coupling could not be included. In addition, a smaller basis set was employed, which only had minor effects on the relative energies of the involved states at critical

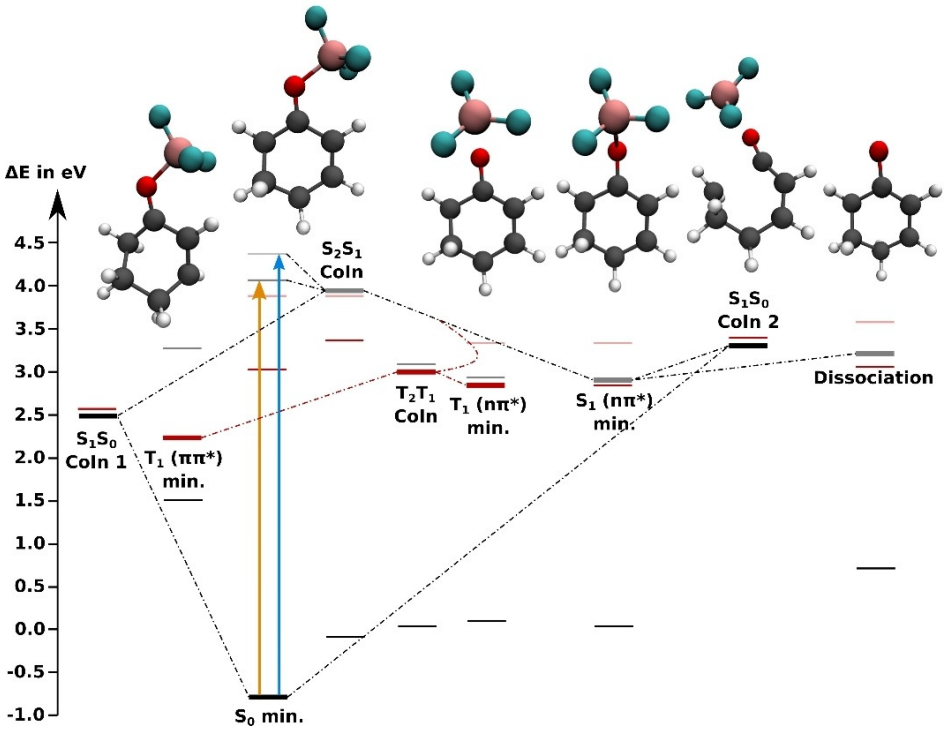

Figure 6. Energy levels of the adiabatic states of **2** at critical points relevant to the relaxation process evaluated at XMS-CASPT2(8,7)/cc-pvdz level of theory. S_0 is shown in black, S_1 in grey and S_2 in faint grey; T_1 is shown in red and T_2 in faint red. The thick horizontal lines indicate the energies of the optimized states, while the thin lines indicate the energies of all other states at the optimized geometries (see Tables S15–S20). The dotted lines suggest possible relaxation pathways. The molecular structures are (from left to right): The twisted $T_1(\pi\pi^*)$ minimum (torsion around the C–C double bond), the FC geometry, the $T_1(n\pi^*)$ and $S_1(\pi\pi^*)$ minima with the torsion around the C–O double bond and the elongated O–B bond, the ring opening CoIn between S_1 and S_0 and the S_1 minimum of free 2-cyclohexenone (**1**) that is reached by dissociation in the S_1 state.

points of the potential energy surface (see Tables S16 and S19). While dynamics in the singlet states can only provide a part of the picture, it was possible to investigate a larger number of trajectories. In total 50 trajectories per conformer and initial state were run. The results differed depending on whether the trajectories were started in the $S_1(n\pi^*)$ state or the $S_2(\pi\pi^*)$ state. Starting from S_1, most trajectories led to dissociation, since by removing an electron from the n-orbital the oxygen-boron bond is weakened so that the energy gained by relaxation from the FC region is enough to break it. Eleven trajectories did not dissociate. All of them showed a hop from S_1 to S_0 early in the propagation. In total, we observed thirteen hops from S_1 to S_0, of which eleven happened at a twisted structure (S_1S_0 CoIn 1) while two occurred at an open ring structure (S_1S_0 CoIn 2). Interestingly, there was a significant difference between the two conformers of the complex. When the BF_3 was on the same side as the double bond (**2**), the relaxation mainly proceeded through S_1S_0 CoIn 1. When the BF_3 pointed away from the double bond (**2′**), dissociation was more likely, and relaxation mainly proceeded through S_1S_0 CoIn 2. The population dynamics of the trajectories starting in S_2 is shown in Figure 7. In this case, the difference between the two conformers was small. All trajectories quickly relaxed to S_1, but from there, different pathways were taken. 34 Trajectories relaxed to the S_0 state, 30 of them hopped at a twisted structure similar to the S_1S_0 CoIn 1. In general, these trajectories did not show dissociation. They followed the electronic ππ* character diabatically. The other four hops occurred at an open-ring structure similar to S_1S_0 CoIn 2 and contained a broken or very elongated oxygen-boron bond. Due to these accessible relaxation channels we see a re-population of the S_0 ground state on a time scale below 150 fs. The remaining 66 trajectories stayed in the S_1. These trajectories follow the nπ* character diabatically and mainly show dissociative behavior in the gas phase. In solution, caging effects could decelerate or even prevent the dissociation.[23]

Transient Absorption Spectra. We experimentally addressed the photoinduced dynamics of compound **2** on timescales commensurate with intramolecular electronic relaxation using femtosecond TA spectroscopy. We initiated excited-state dynamics by pulses centered at 285 nm, to predominantly excite the $S_0 \rightarrow S_1$ transition, and followed the time-evolution by UV and UV/Vis probe pulses. A representative selection of TA spectra is shown in Figure 8, where the spectral evolution over the first several picoseconds after excitation is clearly illustrated.

Over the time-range displayed here, substantial changes were observed in particular in the visible: immediately on

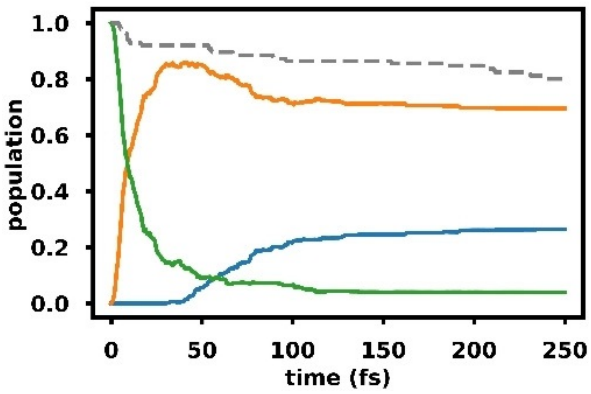

Figure 7. Adiabatic state populations based on Boltzmann averaged quantum amplitudes for XMS-CASPT2(8,7)/cc-pvdz surface hopping trajectories started in the S_2 state of **2** and **2′**; S_2 (green), S_1 (orange), S_0 (blue); Boltzmann weighted fraction of active trajectories of **2** and **2′** (grey, dashed).

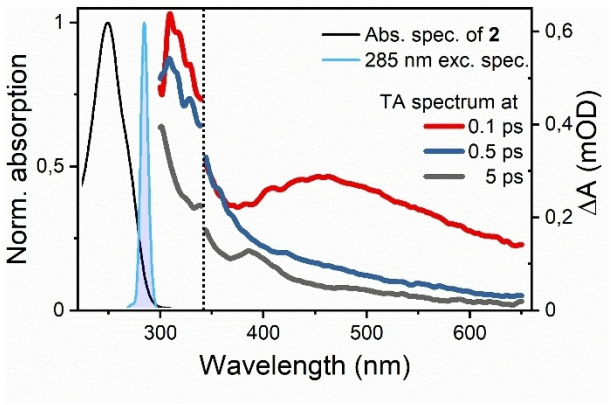

Figure 8. Normalized absorption (black line), excitation spectra (blue shaded area) and TA spectra of **2** at several time-delays (colored lines). TA spectra in the UV ($\lambda < 340$ nm) and Visible ($\lambda > 340$ nm) range were recorded in separate experiments.

excitation, a broad visible excited-state absorption (ESA) band covering 400–600 nm was formed. This band subsequently decayed on a timescale of a few hundred femtoseconds, revealing rapid population transfer out of the initially excited FC region. Following this initial process, subtler changes, as well as an overall loss of signal intensity, took place across the UV/Vis spectral range over the next several picoseconds. Figure 9 displays the (normalized) TA maps in two-dimensional detection wavelength vs. time-delay plots.

The initial ≈ 100 fs of the dynamics are dominated by the coherent artifact (CA), inhibiting detailed analysis within this range. After the CA, however, the spectra were well behaved and revealed the relaxation dynamics on the excited state surface. Again, we saw a broad ESA feature characterizing the excited state at the FC point. This band rapidly decayed, leaving only a weak featureless ESA in the visible range as well as a more intense band in the UV. These bands decayed much more slowly, reaching a quasi-equilibrium state after a few picoseconds as demonstrated by the transients at UV and visible detection wavelengths in Figure 9b. TA spectra from experiments recorded using 260 nm excitation, displaying similar behavior, are shown in Figures S1 and S2. Note that long-lived oscillatory features were observed across the spectrum regardless of detection wavelength, but with highest amplitude at 340 nm as shown in Figure 9b. These oscillations are not related to intra-molecular dynamics of the studied complex but are rather impulsive stimulated Raman scattering features originating from the solvent (see Figure S4 for pure solvent spectra).

Kinetic Model and Data Analysis. We can extract quantitative information about the excited-state relaxation dynamics by simultaneously fitting the time-evolution of the signal at all detection wavelengths to a sum-of-exponentials decay model (sequential model, see below), using the time constants as global parameters. A purely sequential model ($A \rightarrow B \rightarrow C\ldots$) is one of the simplest deactivation schemes, which is however also supported by the theoretical model in Figure 6. From a physical perspective, we expect a bifurcation of the S_1 population via $S_1 \rightarrow S_0$ and $S_1 \rightarrow T_1$. We do not expect to observe the former channel directly, that is, the formation of a vibrationally hot ground state, as the TA probing range does not cover the ground state bleach region (see Figure 9 in comparison to the absorption spectrum in Figure 8). For the remaining and spectrally observable reaction pathway, $S_1 \rightarrow$

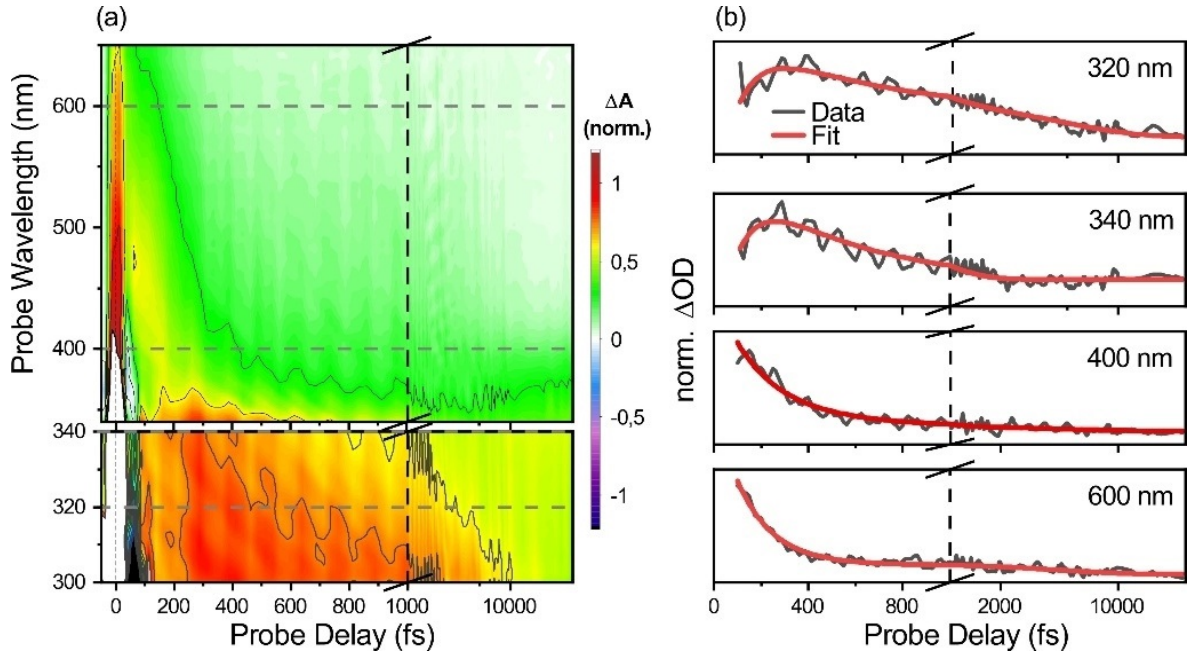

Figure 9. (a) Transient absorption maps for **2** DUV (bottom) and UV/Visible (top) probe range spectra after 285 nm excitation. Spectra are normalized to the signal maximum in the DUV experiment. Time-scale changed to logarithmic at 1 picosecond. (b) Transients at indicated detection wavelengths (dark grey) in comparison to fit results from global analysis (red). Spectra at each detection wavelength are normalized to their respective maximum.

T_1, theory predicts a uni-directional relaxation, for which a purely sequential model is a good approximation. Singular value decomposition and inspection of the resulting fit residuals reveals that four time constants suffice to explain the photodynamics after 285 nm excitation. All time constants are collected in Table 2.

Table 2: Collected time constants extracted from global kinetic analysis of the transient absorption experiments. The longest living component (corresponding to the ground-state recovery) has a decay-time longer than the measurement time window.

	Component	Lifetime in ps
DUV probe	τ_1	0.10
	τ_2	0.45
	τ_3	4.8
	τ_4	>50
VIS probe	τ_1	0.16
	τ_2	0.30
	τ_3	4.4
	τ_4	>50

The fastest component in the TA data decays on a 100–150 fs timescale and is readily attributed to rapid decay of the initially excited FC state, while the ground-state recovery at long times proceeds on timescales longer than our probe window (i.e. >50 ps). At intermediate times, the picture is less clear, at least before a comparison with the theoretical studies was made as given in the next section. We observe two components with sub-ps and few ps dynamics.

In addition to the time constants of the components in a multi-exponential decay fit, it is useful to represent also their amplitudes. A spectral representation of these reveals detailed information about the probe wavelengths at which a given process contributes. While a number of spectral representations are possible, we here show the *Evolution Associated Decay Spectra* (EADS)[24] in Figure 10 (time constants and EADS from 260 nm excitation experiment shown in Figure S3). The physical model imposed on the data in this representation is a strictly sequential transfer between a set of "compartments", where the EADS can be interpreted as the transient spectra of the individual compartments. As such, the population is initially found in "compartment 1", whereafter it transfers to "compartment 2", and so on.

The EADS in Figure 10 renders our qualitative observations quantitative regarding the raw data in Figure 9. The initially excited state displays a broad ESA across the visible spectrum. As it decays on a $\approx$130 fs time-scale, a spectrally distinct state—characterized largely by strong UV absorption—is formed. Subsequently, on timescales from several hundred fs to a few ps, we observe signal loss and small-scale spectral changes largely in the UV range between 300 and 400 nm.

Overall, these spectral dynamics are consistent with initial excitation, followed by rapid transfer into a manifold of states, where the electronic structure is substantially different. In the following section, these assignments are substantiated significantly by a theoretical analysis of excited state spectra.

Excited State Spectra—Experiment vs. *Theory.* The theoretical approaches discussed so far describe processes connected to the optical excitation (Figures 2 and 3), and the subsequent population relaxation processes including non-adiabatic coupling and ISC (Figures 4–7). As XMS-CASPT2 can also accurately capture higher lying excited states, it further provides a direct connection between populations and spectral observables through calculated ESA spectra (the calculation of the ESA spectra is described in the Computational Methods section of the supporting information). This in turn greatly facilitates the discussion of the experimental results, as the EADS in Figure 10 can now be assigned to specific excited states and molecular geometries by comparison with calculated ESA features. In Figure 11 we compare the calculated ESA spectra of S_1 in the FC region and T_1 in the

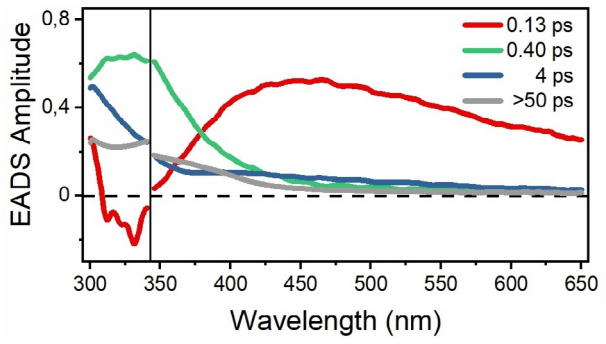

Figure 10. Evolution associated decay spectra extracted from global kinetic analysis of TA data after excitation at 285 nm. The time constants noted are approximate representations of parameters extracted from both UV and visible experiments—the actual time constants from a given dataset can be found in Table 2.

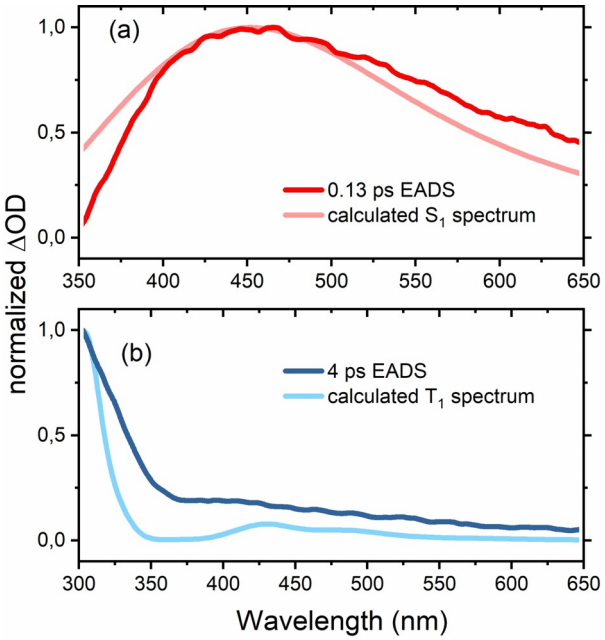

Figure 11. Comparison between selected EADS (full colors) and calculated ESA spectra (faint colors) of singlet state S1 of **2**/**2′** in the FC region (a) and triplet state T1 thermalized in the T1($\pi\pi^*$) minimum (b).

$T_1(\pi\pi^*)$ minimum to relevant EADS. Based on the fact that S_1 may deactivate both towards S_0 (see Figure 7 for population dynamics of **2**) and to the triplet states T_1 and T_2, we expect its overall lifetime to be short. Accordingly, comparison of the fastest decaying EADS component with a 0.13 ps lifetime (red curve in Figure 11 (a)) with the calculated ESA spectrum of S_1 in the FC region (faint red curve) gives qualitatively excellent agreement. The calculated spectrum is the sum of three transitions, that is, $S_1 \rightarrow S_{2,3,4}$, where we depict their relative weights and the analogous decomposition of the T_1 ESA spectrum in Figures S11 and S10, respectively. The minor deviation between experiment and theory in Figure 11 (a) in the spectral regions below 400 nm is readily explained by the pump pulse-related CA, still contributing significantly at such early delay times.[25] Thus we can assign the fastest decay component to the relaxation of S_1 out of the FC region either to the ground-state S_0 through conical intersections or to the $S_1(n\pi^*)$ minimum.

The triplet state T_1 is the lowest lying excited state of **2** (see Figure 6). Hence, we compare the calculated ESA spectrum in the $T_1(\pi\pi^*)$ minimum (blue faint line in Figure 11 (b)) to the component with a long lifetime—specifically the 4 ps EADS (blue line). Even though we retrieved a component with an even longer lifetime (see Figure 9), we chose to compare to the 4 ps EADS, as this component's lifetime is still reliable within the 50 ps delay window of the experiment. As for the S_1 case, the qualitative agreement between experiment and theory is remarkable (Figure 11 (b)). We note that the results of global analysis, that is, EADS, relate to the entire TA-signal, while the theoretical predictions were made for ESA spectra only. The direct comparison of the calculated ESA-spectra to the retrieved EADS is only feasible thanks to the lack of ground state bleach contributions in the employed probing range of Figure 11 and to the weak stimulated signal for both S_1 and T_1. Comparison to theory hence allows us to assign the retrieved spectral species of Figure 9 to relaxation out of the FC region of S_1 (0.13 ps EADS), ISC to triplet states (0.4 ps), relaxation of hot triplet states (4 ps) and a long-lived residual (>50 ps), which is attributable to the lowest lying triplet state T_1 and its relaxation back to the ground state. The excellent agreement of the calculated triplet spectrum and the 4 ps EADS strongly suggests that the dissociation that is predicted by surface hopping calculations in the gas phase is not a large contributor to the dynamics of **2** in solution. The triplet spectra of **1** which would result from dissociation, were also calculated and do not match the observed EADS but are instead much more red-shifted (see Figure S12).

Preliminary studies on photoreactivity. Our results indicate that it should be possible to involve enones in a photochemical Lewis acid-catalyzed reaction upon proper selection of the irradiation wavelength. While complexation opens up additional relaxation pathways which avoid the photochemically relevant triplet state, these additional decay routes are non-critical, as they lead back to the electronic ground state. Hence, there are no chemical by-products and the complex remains in solution for further photocatalytic cycles. By appropriate choice of the excitation wavelength, it should therefore be possible to compensate for the loss of reactive excited state species by an increased absorption cross section.

In a preliminary study, we investigated whether the BF_3 complex **2** is productive in photocatalysis. 2-Cyclohexenone (**1**) was irradiated together with isobutene at a wavelength ($\lambda = 272$ nm) at which the compound is transparent (see Figure 1). There was no detectable conversion after six hours (see section 7 of the SI for details). When the same reaction was performed in the presence of $BF_3{\cdot}OEt_2$ (50 mol%) a steady conversion could be detected (see Figure S13). In the absence of light there was no reaction. This preliminary work supports the fact that the triplet state of **2** is productive in photocatalysis and suggests Lewis acid catalyzed photochemical reactions to be possible upon judicious choice of the irradiation wavelength.

Conclusion

In summary, we have investigated the small enone Lewis acid complex **2** by highly accurate quantum chemical methods and by state-of-the art ultrafast transient absorption spectroscopy in the UV-range. The complex serves as a prototype to understand the influence of Lewis acid catalysts on the photochemistry of cyclic enones. The changes due to complexation were evaluated by comparison with the free enone **1**. Regarding absorption in the UV/Vis spectrum, the Lewis acid induces a significant blue shift of the S_1 state and increases its oscillator strength. The S_1 state is almost dark for enone **1** but becomes bright for complex **2**. The bright S_2 state of the enone is red-shifted by the Lewis acid and overlaps energetically with S_1. While the enone decays from S_1 completely to the triplet ($n\pi^*$) and ($\pi\pi^*$) states, the enone complex **2** passes conical intersections at which a decay to the ground state S_0 is feasible. An alternative pathway allows the enone complex to populate the triplet $T_1(\pi\pi^*)$ state. Both the S_1 and T_1 state of complex **2** could be detected by transient absorption spectroscopy and it was shown that coordination to the Lewis acid is retained in T_1. The latter observation is in line with the fact that chiral boron-based Lewis acids induce a high enantioselectivity in the [2+2] photocycloaddition reaction of 2-cyclohexenone.[26] Population of T_1 occurs on a picosecond time scale which in turn suggests that this state is solely responsible for the photochemistry of the Lewis acid-enone complex. Further synthetic studies are warranted to identify novel reaction pathways for Lewis acid-enone complexes as compared to the known transformations of enones.

Acknowledgements

Financial support by the European Research Council under the European Union's Horizon 2020 research and innovation programme (grant agreement No 665951—ELICOS) is gratefully acknowledged. R.dVR and J.H. acknowledge funding by DFG under Germany's ExcellenceStrategy-EXC 2089/1–390776260. D.P.S. thanks *Studienstiftung des deutschen Volkes* for a Ph.D. fellowship, S. Breitenlechner (TUM) for fruitful discussions and J. Kudermann (TUM) for his help with GLC

analyses. Open access funding enabled and organized by Projekt DEAL.

Conflict of interest

The authors declare no conflict of interest.

Keywords: calculations · enones · lewis acids · photochemistry · time-resolved spectroscopy

[1] a) P. Praetorius, F. Korn, *Ber. Dtsch. Chem. Ges.* **1910**, *43*, 2744 – 2746; b) F. H. Stobbe, E. Färber, *Ber. Dtsch. Chem. Ges.* **1925**, *58*, 1548 – 1553.
[2] a) S. C. Shim, E. I. Kim, K. T. Lee, *Bull. Korean Chem. Soc.* **1987**, *8*, 140 – 144; b) T. Ogawa, Y. Masui, S. Ojima, H. Suzuki, *Bull. Chem. Soc. Jpn.* **1987**, *60*, 423 – 425; c) S. C. Shim, S. S. Lee, *Bull. Korean Chem. Soc.* **1989**, *10*, 324 – 326.
[3] Most recent contributions from the series: a) F. D. Lewis, S. V. Barancyk, E. L. Burch, *J. Am. Chem. Soc.* **1992**, *114*, 3866 – 3870; b) F. D. Lewis, G. D. Reddy, J. E. Elbert, B. E. Tillberg, J. A. Meltzer, M. Kojima, *J. Org. Chem.* **1991**, *56*, 5311 – 5318.
[4] a) S. Fukuzumi, T. Okamoto, J. Otera, *J. Am. Chem. Soc.* **1994**, *116*, 5503 – 5504; b) S. Fukuzumi, N. Satoh, T. Okamoto, K. Yasui, T. Suenobu, Y. Seko, M. Fujitsuka, O. Ito, *J. Am. Chem. Soc.* **2001**, *123*, 7756 – 7766.
[5] For a recent review, see: S. Fukuzumi, J. Jung, Y.-M. Lee, W. Nam, *Asian J. Org. Chem.* **2017**, *6*, 397 – 409.
[6] Recent reviews: a) C. Prentice, J. Morrisson, A. D. Smith, E. Zysman-Colman, *Beilstein J. Org. Chem.* **2020**, *16*, 2363 – 2441; b) T. Rigotti, J. Alemán, *Chem. Commun.* **2020**, *56*, 11169 – 11190; c) C. Brenninger, J. Jolliffe, T. Bach, *Angew. Chem. Int. Ed.* **2018**, *57*, 14338 – 14349; *Angew. Chem.* **2018**, *130*, 14536 – 14547.
[7] H. Guo, E. Herdtweck, T. Bach, *Angew. Chem. Int. Ed.* **2010**, *49*, 7782 – 7785; *Angew. Chem.* **2010**, *122*, 7948 – 7951.
[8] J. Du, K. L. Skubi, D. M. Schultz, T. P. Yoon, *Science* **2014**, *344*, 392 – 396.
[9] R. Brimioulle, T. Bach, *Science* **2013**, *342*, 840 – 843.
[10] T. R. Blum, Z. D. Miller, D. M. Bates, I. A. Guzei, T. P. Yoon, *Science* **2016**, *354*, 1391 – 1395.
[11] X. Huang, T. R. Quinn, K. Harms, R. D. Webster, L. Zhang, O. Wiest, E. Meggers, *J. Am. Chem. Soc.* **2017**, *139*, 9120 – 9123.
[12] a) N. Hu, H. Jung, Y. Zheng, J. Lee, L. Zhang, Z. Ullah, X. Xie, K. Harms, M.-H. Baik, E. Meggers, *Angew. Chem. Int. Ed.* **2018**, *57*, 6242 – 6246; *Angew. Chem.* **2018**, *130*, 6350 – 6354; b) S. Stegbauer, C. Jandl, T. Bach, *Angew. Chem. Int. Ed.* **2018**, *57*, 14593 – 14596; *Angew. Chem.* **2018**, *130*, 14801 – 14805; c) S. Stegbauer, N. Jeremias, C. Jandl, T. Bach, *Chem. Sci.* **2019**, *10*, 8566 – 8570; d) J. Ma, F. Schäfers, C. Daniliuc, K. Bergander, C. A. Strassert, F. Glorius, *Angew. Chem. Int. Ed.* **2020**, *59*, 9639 – 9645; *Angew. Chem.* **2020**, *132*, 9726 – 9732.
[13] M. Leverenz, C. Merten, A. Dreuw, T. Bach, *J. Am. Chem. Soc.* **2019**, *141*, 20053 – 20057.
[14] S. Poplata, A. Bauer, G. Storch, T. Bach, *Chem. Eur. J.* **2019**, *25*, 8135 – 8148.
[15] a) H. Wang, X. Cao, X. Chen, W. Fang, M. Dolg, *Angew. Chem. Int. Ed.* **2015**, *54*, 14295 – 14298; *Angew. Chem.* **2015**, *127*, 14503 – 14506; b) H. Wang, W.-H. Fang, X. Chen, *J. Org. Chem.* **2016**, *81*, 7093 – 7101.
[16] D. I. Schuster, D. A. Dunn, G. E. Heibel, P. B. Brown, J. M. Rao, J. Woning, R. Bonneau, *J. Am. Chem. Soc.* **1991**, *113*, 6245 – 6255.
[17] a) E. García-Expósito, M. J. Bearpark, R. M. Ortuño, V. Branchadell, M. A. Robb, S. Wilsey, *J. Org. Chem.* **2001**, *66*, 8811 – 8814; b) E. García-Expósito, M. J. Bearpark, R. M. Ortuño, M. A. Robb, V. Branchadell, *J. Org. Chem.* **2002**, *67*, 6070 – 6077.
[18] A. M. D. Lee, J. D. Coe, S. Ullrich, M.-L. Ho, S.-J. Lee, R.-M. Cheng, M. Z. Zgierski, I.-C. Chen, T. J. Martinez, A. Stolow, *J. Phys. Chem. A* **2007**, *111*, 11948 – 11960.
[19] O. Schalk, M. S. Schuurman, G. Wu, P. Lang, M. Mucke, R. Feifel, A. Stolow, *J. Phys. Chem. A* **2014**, *118*, 2279 – 2287.
[20] J. Cao, Z.-Z. Xie, *Phys. Chem. Chem. Phys.* **2016**, *18*, 6931 – 6945.
[21] R. F. Childs, D. L. Mulholland, A. Nixon, *Can. J. Chem.* **1982**, *60*, 801 – 808.
[22] M. A. El-Sayed, *Acc. Chem. Res.* **1968**, *1*, 8 – 16.
[23] S. Thallmair, M. Kowalewski, J. P. P. Zauleck, M. K. Roos, R. de Vivie-Riedle, *J. Phys. Chem. Lett.* **2014**, *5*, 3480 – 3485.
[24] I. H. M. van Stokkum, D. S. Larsen, R. van Grondelle, *Biochim. Biophys. Acta Bioenerg.* **2004**, *1657*, 82 – 104.
[25] V. Perlík, J. Hauer, F. Šanda, *J. Opt. Soc. Am. B* **2017**, *34*, 430 – 439.
[26] S. Poplata, T. Bach, *J. Am. Chem. Soc.* **2018**, *140*, 3228 – 3231.

Manuscript received: December 15, 2020
Revised manuscript received: February 1, 2021
Accepted manuscript online: February 17, 2021
Version of record online: March 23, 2021

